Desalination and Water Treatment
www.deswater.com
doi: 10.5004/dwt.2021.27775

241 (2021) 51–63
November

A three-dimensional model for the heat and mass transfer in air-gap membrane distillation

Kerstin Cramer[a], Bojan Niceno[b], Horst-Michael Prasser[c], Stephan Leyer[a,*]

[a]*University of Luxembourg, 1359 Luxembourg, Luxembourg, emails: kerstin.cramer@uni.lu (K. Cramer), stephan.leyer@uni.lu (S. Leyer)*
[b]*Paul-Scherrer-Institute (PSI), 5232 Villigen, Switzerland, email: bojan.niceno@psi.ch*
[c]*Swiss Federal Institute of Technology (ETHZ), 8092 Zürich, Switzerland, email: prasser@lke.mavt.ethz.ch*

Received 10 April 2020; Accepted 26 August 2021

ABSTRACT

Membrane distillation (MD) is a process to desalinate sea water. Pilot plants are operated aiming at increasing the modules' efficiency for large-scale applications. In air-gap membrane distillation (AGMD) the state-of-the-art modeling of mass and heat transfer is one-dimensional, combining evaporation and diffusion through the membrane and the condenser channel in one correlation. In this work, a numerical model is developed which computes AGMD modules in three dimensions. For evaporation and condensation, energy conservation equations at the interfaces are solved. Simulation results are compared to experimental data and a good agreement is found. The model is then employed to compare numerically two air-gap MD module configurations and evaluate their performance at different feed inlet temperatures, velocities and air-gap thicknesses. In the upside configuration, the hot feed flows above the membrane, while in the downside configuration it flows below the air-gap and membrane. In the latter, the feed solution is not in contact with the membrane but separated by the air-gap which is expected to improve the fouling resistance of the membrane. The three-dimensional computational fluid dynamic computation allows the visualization of the velocity profile in the air-gap due to buoyancy in the downside configuration.

Keywords: Numerical modeling; Heat and mass transfer; Temperature polarization; Seawater desalination; Computational fluid dynamic; Natural convection

1. Introduction

Fresh water supply is a problem in large parts of the world. According to World Health Organization (WHO), 3.5 million fatalities occur each year due to a lack of fresh drinking water while the trend is rising due to population growth [1]. Membrane distillation (MD) is considered a promising desalination technique that requires low-grade heat to thermally separate potable water from the sea or brackish water [2]. Other advantages include a large insensitivity to feed concentration, a high quality of produced fresh water and a higher fouling resistance than other comparable desalination techniques [3]. Despite its advantages, MD lacks the energy efficiency and the economical performance to be competitive in commercial applications [4]. Membrane distillation uses renewable energy or waste heat to desalinate feed water by generating a temperature gradient between hot salt water and colder fresh water, which are separated by a membrane. The membrane is filled with air and is hydrophobic but permeable to water vapor. Thereby, the temperature gradient leads to a gradient in partial vapor pressure across the membrane. It drives the evaporation of water at the liquid–vapor interface on the membrane top at temperatures below the boiling point. Salt is not soluble in water vapor and is therefore retained in liquid water. Desalinated water is mostly produced by

* Corresponding author.

condensing the water vapor either directly into a fresh water stream (direct contact membrane distillation) or into a cooled, air-filled condenser compartment forming a liquid film at the bottom (air-gap membrane distillation). Other configurations are realized as well. Direct contact membrane distillation (DCMD) is the most studied configuration [5], while air-gap membrane distillation (AGMD) is the configuration applied in most pilot plants [4]. In DCMD a significant amount of heat is lost via conduction through the membrane which is not used to evaporate water vapor as desired. The insulating air-gap in AGMD reduces the conductive heat flow in the module while introducing an additional mass resistance to the vapor flux. Still, performance is improved if the air-gap is kept small [6]. A phenomenon observed in all configurations is temperature and concentration polarization. A strong temperature and concentration gradient are observed in the boundary layer of the feed stream at the membrane [7]. It is assumed to be the limiting factor for transport efficiency [8].

One-dimensional heat and mass transfer models were developed for DCMD computing the membrane flux and heat transfer through the membrane from the bulk flow parameters under consideration of temperature polarization [9]. For AGMD, the mass transfer through membrane and air-gap is combined in a one-dimensional equation [10,11]. Summers et al. [12] extended these models to two dimensions in the hot feed and air-gap channel to compare different MD configurations with respect to their energy efficiency. The authors concluded that AGMD and DCMD have the potential for high energy efficiency in comparison to vacuum MD and that in AGMD the air-gap thickness has the highest impact on energy efficiency. Alklaibi and Lior [13] developed a very detailed model for an AGMD hollow fiber module. The temperature profile in the hot water channel, air-gap, liquid film, cooling plate and coolant channel is solved in two dimensions. The liquid film thickness is calculated assuming the condensation mass flux equal to the vapor flux through the membrane which is calculated using the molecular diffusion model. Thereby, mass diffusion in the air-gap is still one-directional neglecting multi-dimensional influences on the vapor mass flow which are otherwise solved for in the conservation equations. The radial temperature profile and boundary layer at different axial locations are shown indicating temperature variations in the axial direction. The authors identify the air-gap thickness and hot feed inlet temperature as very influential for permeate flux and energy efficiency while cooling channel and feed velocity are less influential. They also confirm the insulating effect of the air-gap and evaluate the heat resistance of the liquid film and bottom plate negligible. Chouikh et al. [14] computed natural convection in the air-gap in two dimensions solving steady-state elliptic transport equations. They found that natural convection was occurring and enhancing the vapor flux through the membrane (up to 30%), however, a constant hot feed and coolant temperature was applied as boundary condition not taking into account axial temperature profiles as shown by Summers et al. [12] and Alklaibi and Lior [13]. Xu et al. [15] study the feed channel in AGMD in two dimensions using the commercial software FLUENT. They show that an increasing Reynolds number in the feed flow increases also permeate flux and reduces temperature polarization. Similarly, Orfi et al. [16] present an AGMD model which computes the feed channel in two dimensions accounting for slip flow. The model is in good agreement with experimental data and the slip flow was found beneficial for process parameters like heat transfer and thermal efficiency. In both studies, the air-gap is computed using one-dimensional correlations. Janajreh et al. [17] presented the axial profiles of temperature, temperature polarization, permeate mass flux and thermal efficiency in different DCMD configurations. In their study, the Navier–Stokes and energy equations are solved in two dimensions using commercial software FLUENT assuming Knudsen diffusion and Poiseuille flow through the membrane as in Schofield's model [18]. In a different study, they extend the model to AGMD and also compute the temperature and velocity profiles in the air-gap, however, the permeate flux is calculated as the flux through the membrane assuming saturated air conditions on both sides of the membrane [19]. Thereby, condensation processes are not modeled and influences on mass transfer in the air-gap on the vapor flux are neglected. The authors conclude that temperature polarization is reduced in AGMD compared to DCMD as is the thermal efficiency and the permeate flux. In AGMD modeling, evaporation and condensation modeling as well as detailed heat and mass transfer in the air-gap has seen little attention so far, even though natural convection has been shown.

The three-dimensional analyses of processes in membrane distillation are relatively few but gaining interest [20–22]. In Tang et al. [23], authors used computational fluid dynamic (CFD) to simulate membrane distillation of aqueous NaCl solutions in two-dimensional domains using commercial software FLUENT and the results they obtained are consistent with experimental findings. Still assuming two-dimensional geometry, authors in Yang et al. [24] analyzed the effect of turbulence promoters in hollow fiber membrane distillation and have found that the efficiency of the process can be increased more than 50% if operated in a turbulent flow regime, whereas heat flux can increase six times. A three-dimensional analysis of membrane module in DCMD is described in Chong et al. [25]. The authors focused on the performance of various multiphase models to predict processes in the membrane and conclude that CFD can lead to a huge saving in the time needed to design DCMD modules. A CFD study of vacuum membrane distillation for water desalination is reported in Hayer et al. [26]. The authors used the commercial package COMSOL and find out that the maximum error obtained from their numerical model is 15%. Another work reporting CFD analysis of DCMD is given in Hasanizadeh et al. [27]. To improve the accuracy of their simulations, authors use a composition of Poiseuille and Knudsen diffusion coefficient. Satisfactory agreement is reported on the comparison of CFD results against experiments (average error less than 5%). The work in Chang et al. [28] shows results of three-dimensional CFD simulation of the direct contact DCMD modules with and without rough surface channels for desalination. The authors report close agreement with experimental findings (less than 10% error) for cases in which one-dimensional correlations fail. A work that reports usage of CFD analysis

with commercial software Star-CCM+ on performance assessment of permeate gap MD is given in Yazgan-Birgi et al. [29]. The authors relied on a realizable $k-\varepsilon$ turbulence model and report close agreement with the experiment. These studies show the interest and need for multi-dimensional analyses in different MD configurations.

Warsinger et al. [30] assessed the impact of the inclination angle on the AGMD module's energy efficiency and permeate output. Experimentally and numerically, their module was tilted up to 90° from the vertical position in both directions normal to the membrane. They reported an increase in membrane flux in the experiments for both horizontal configurations which they explain with flooding of the air-gap in one case and permeate falling back from the condensation plate onto the membrane in the other. Numerically, the membrane mass flux is also predicted to increase from vertical to horizontal configuration. The change in orientation is considered in the calculation of the condensate film thickness which is increased when orienting the module horizontally in either direction. The computation is therefore invariant to the direction of the temperature gradient across the module and gravitational effects are not included.

Tan et al. [31] studied the influence of the orientation of DCMD on the permeate flux. They concluded that for desalination the hot water channel below the membrane performed best whereas for the treatment of oily feeds the exact opposite configuration is preferred. The findings are mainly based on their experiments as their simulations are performed isothermally.

In this work, a three-dimensional model for flat-sheet AGMD is presented which allows studying three-dimensional heat and mass transfer processes not only in the feed channel but also in the air-gap. Special emphasis is put on the heat and mass transfer modeling of the evaporation and condensation processes, which received little attention in other studies. At the liquid–vapor interfaces, conjugate heat transfer models are applied satisfying the energy conservation to determine interface temperatures. They allow for the independent calculation of the vapor flux evaporating from the hot feed into the membrane and condensing vapor flux at the liquid film. The model is compared to experimental data published by Banat [32] which have been previously used for numerical validation [13].

The model is used to investigate the influence of module orientation on energy efficiency and performance. Therefore, two horizontal AGMD module designs are analyzed in which the hot feed water flows above the membrane in the first and below the membrane in the other. In the later orientation, convection phenomena due to buoyancy effects and their impact on the heat and mass transfer are investigated. Different operation conditions and air-gap thicknesses are compared numerically.

2. Numerical model

The model computes the hot feed channel, air-gap, liquid film and cooling channel in three dimensions. Thereby, the conjugate heat transfer model is employed. In between, the evaporation interface, membrane, condensation interface and cooling plate are considered with one-dimensional heat and mass transfer correlations applied to individual computational cells. A graphical representation of the modeled AGMD module and relevant temperature locations can be found in Fig. 1. In the following, the equations, assumptions and boundary conditions are presented.

2.1. Hot feed channel

The Navier–Stokes (NS) and energy conservation equation are solved in three dimensions [Eqs. (1)–(3)]. Eq. (2) displays the pressure correction equation which is needed to satisfy mass conservation. Gravity is considered in the force term F. Additionally, a concentration conservation equation is solved for the salt concentration a_s [Eq. (4)].

$$\int_V \frac{\partial \rho \mathbf{u}}{\partial t} dV + \int_S \rho \mathbf{u}\mathbf{u} d\mathbf{S} = \int_S \mu \nabla \mathbf{u} d\mathbf{S} + \int_V \nabla P dV + \mathbf{F} \tag{1}$$

$$\int_S \frac{\nabla P'}{\rho} d\mathbf{S} = \frac{1}{\Delta t} \int_S \mathbf{u} d\mathbf{S} \tag{2}$$

$$\int_V \frac{\partial \rho c_p T}{\partial t} dV + \int_S \rho \mathbf{u} c_p T d\mathbf{S} = \int_S \lambda \nabla T d\mathbf{S} \tag{3}$$

$$\int_V \frac{\partial \rho a_s}{\partial t} dV + \int_S \rho \mathbf{u} a_s d\mathbf{S} = \int_S D_{s,H_2O} \nabla a_s d\mathbf{S} \tag{4}$$

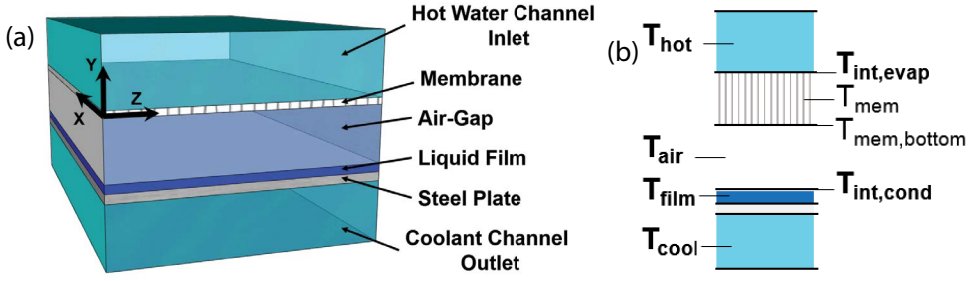

Fig. 1. (a) Domains included in the model (not to scale); heat and mass transfer through the membrane and heat transfer through the steel plate are calculated in one-dimensional, the other domains in three-dimensional and (b) relevant temperature locations and their naming convention.

where **u** denotes velocity, ρ density, μ dynamic viscosity, P pressure, P' pressure correction, T temperature, λ thermal conductivity, c_p heat capacity and D_{s,H_2O} is the diffusion coefficient of salt in water.

The temperature at the inlet is assumed to be constant and uniform. The walls are modeled as adiabatic. For the temperature on the boundary to the membrane, the interface saturation temperature $T_{int,evap}$ is applied which is calculated from the energy jump condition as described in Section 2.2.

At the membrane side, a velocity component normal to the membrane is computed as $v = \dot{m}_D / \rho_{H_2O}$ from the membrane vapor flux and the density of the feed water.

2.2. Evaporation interface and membrane

2.2.1. Energy conversation at the interface

The energy conversation at the interface is developed for the modeling of multiphase flows and combines the heat and mass transfer including the latent heat across a liquid–vapor interface. It dictates that all heat fluxes transferred from the liquid to the interface must leave the interface either by conduction to the vapor phase or evaporation as the interface has no thermal inertia. This is illustrated in Fig. 2 and translates into Eq. (5) where the simplified temperature naming of Fig. 2 is applied.

$$\dot{q}_{l\to int} = \dot{q}_{int\to g} + \dot{m}_{evap} \cdot h_d \tag{5}$$

Fourier's law is used to determine the heat flux from the liquid phase to the interface $\dot{q}_{l\to int}$ and from the interface to the gaseous phase $\dot{q}_{int\to g}$ [Eq. (6)].

$$\dot{q}_{l\to int} = \frac{\lambda_l}{d_l}\left(T_l - T_{int}\right) \tag{6}$$

Combining Eqs. (5) and (6) and applying it on the AGMD module, an equation is obtained which relates the interface temperature $T_{int,evap}$ and the evaporation mass flux at given hot salt water and air-gap temperature [Eq. (7)]. The distance from the point where the hot channel temperature T_{hot} is defined to the interface is only half the cell height $d_{hot}/2$ and therefore the factor 2 needs to be included. The same holds true on the airside. ε denotes the porosity of the membrane.

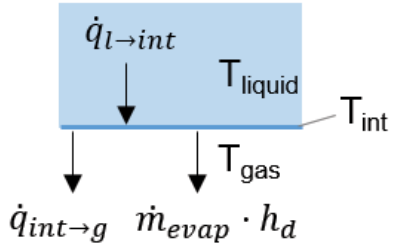

Fig. 2. Illustration of heat fluxes and temperatures at the interface; as there is no thermal inertia in the interface, all heat fluxes must balance out.

$$\dot{m}_{evap} \cdot h_d = \epsilon \frac{2\lambda_{hot}}{d_{hot}}\left(T_{hot} - T_{int,evap}\right) - \epsilon \frac{1}{\frac{d_{mem}}{\lambda_{mem}} + \frac{d_{air}}{2\lambda_{air}}}\left(T_{int,evap} - T_{air}\right) \tag{7}$$

The thermal conductivity of the membrane λ_{mem} is calculated as:

$$\lambda_{mem} = \epsilon \lambda_{air} + \left(1-\epsilon\right)\lambda_{PVDF} \tag{8}$$

2.2.2. Membrane flux

The membrane flux is calculated applying the Dusty–Gas model. The Knudsen number is in the order of unity for the pore diameter and temperature considered and therefore Knudsen and molecular diffusion are considered. Viscous flow can be neglected as the total pressure difference across the membrane is negligible. Membrane flux is calculated according to Eq. (9):

$$\dot{m}_{mem} = -\frac{\epsilon}{\tau R T_{mem}}\left[\left(\frac{2r}{3}\sqrt{\frac{8RT_{mem}M_v}{\pi}}\right)^{-1} + \left(\frac{PM_v D_{v,air}}{p_{air}}\right)^{-1}\right]^{-1} \nabla p \tag{9}$$

where τ as tortuosity, r pore radius, M_v molar mass of vapor, p partial vapor pressure, p_{air} partial pressure of air, P as pressure and $D_{v,air}$ as diffusion coefficient of vapor in the air.

The partial pressure gradient across the membrane is considered between the evaporation interface and the bottom of the membrane where the vapor content is assumed to be equal to the one in the adjacent air cell.

From the ideal gas law and the definition of a_v as the mass fraction of vapor to vapor and air mixture, an expression for the vapor pressure in function of vapor content can be derived [Eq. (10)].

$$p = a_v \frac{M_{tot}}{M_{H_2O}} P, \quad M_{tot} = \frac{1}{\frac{1-a_v}{M_{air}} + \frac{a_v}{M_{H_2O}}} \tag{10}$$

At the interface, the air is assumed to be saturated and the partial vapor pressure p is therefore determined by the Antoine equation from the interface temperature T_{int} [Eq. (11)]. The coefficients are taken from Bridgeman and Aldrich [33] for the corresponding temperature range [Eq. (11)]. The pressure is in the bar and the temperature in K. Raoult's law is applied to account for the boiling point elevation due to the presence of salt [Eq. (12)] where c_s is the mole fraction of salt.

$$\log_{10} p^0_{sat} = \left(A - \frac{B}{T_{int,evap} - C}\right) \tag{11}$$

$$p_{sat} = p_{sat}^{0}\left(1 - c_s\right) \tag{12}$$

By applying the Antoine equation, the membrane flux becomes a function of $T_{int,evap}$ which is not determined at this point. However, both the evaporation interface and the membrane are assumed to have no inertia due to their limited thickness. Thereby, all mass evaporating at the interface must also pass through the membrane to satisfy mass conservation. The evaporation and the membrane mass flux are therefore equal ($\dot{m}_{evap} = \dot{m}_{mem}$). Therefore, Eqs. (7) and (9) can be combined to derive an implicit expression for $T_{int,evap}$.

The temperature in the membrane T_{mem} and at the bottom of the membrane $T_{mem,bottom}$ are then derived using the thermal resistances in a series approach (they are needed for Eq. (9) and the boundary conditions). The partial air pressure and the total pressure in the membrane are calculated as the arithmetic mean value between the interface and the air-gap.

2.3. Air-gap

The NS equations [Eqs. (1)–(3)] are solved for the air-vapor mixture in the air-gap. The temperature boundary condition on the membrane side $T_{mem,bottom}$ is calculated between the air-gap temperature T_{air} and the interface temperature $T_{int,evap}$ according to the thermal resistances in series. In contact with the liquid film, the interface saturation temperature $T_{int,cond}$ is applied as boundary condition as calculated in 2.4.

To account for the vapor, a concentration conservation equation is used to calculate the water content a_v [Eq. (13)].

$$\int_V \frac{\partial \rho a_v}{\partial t} dV + \int_S \rho \mathbf{u} a_v d\mathbf{S} = \int_S D_{v,air} \nabla a_v d\mathbf{S} + J \tag{13}$$

$D_{v,air}$ refers to the diffusion coefficient of water vapor in the air. The vapor mass flux through the membrane $\dot{m}_{mem}$ and the condensation mass flux at the liquid film $\dot{m}_{cond}$ are included in the source term J. The thermodynamic properties of the air vapor mixture are approximated by constant air properties at the mean temperature between hot saltwater inlet temperature and coolant inlet temperature. Only the density is a function of temperature to account for buoyancy effects.

2.4. Condensation interface

The condensation mass flux can be obtained from the energy conservation equation at the interface [Eq. (14)].

$$\dot{m}_{cond} \cdot h_d = \lambda_{film} \frac{\left(T_{int,cond} - T_{film}\right)}{d_{film}/2} - \lambda_{air} \frac{\left(T_{air} - T_{int,cond}\right)}{d_{air}/2} \tag{14}$$

Still, the interface temperature $T_{int,cond}$ is to be determined. For condensation to occur, $T_{int,cond}$ is assumed to be the temperature at which the air in contact with the interface is saturated. Therefore, the vapor pressure in the adjacent air cells is calculated from the vapor content [Eq. (10)] and the inverted Antoine equation is used to determine $T_{int,cond}$ [Eq. (11)].

2.5. Liquid film

The film thickness is kept constant throughout the calculation assuming that the condensation rate equals the condensate discharge from the module. A three-dimensional temperature profile is calculated according to Eq. (3). The boundary temperature on the air side is set to the interface temperature $T_{int,cond}$. On the side of the steel plate, the thermal resistance in a series approach between T_{film} and T_{cool} leads to the temperature boundary condition.

2.6. Coolant channel

In the coolant channel, Eqs. (1)–(3) are solved. Similar to the hot water channel, the temperature at the inlet is assumed to be constant and uniform. The walls are modeled as adiabatic.

3. Implementation

The model is implemented in Python and the finite volume method is used for solving the three-dimensional equations. The first-order backward Euler scheme is applied for temporal discretization, whereas central differencing is used for spatial discretization. Only for the discretization of the advection terms, combined central differencing and upwind schemes are used depending on the velocity gradient across the computational cell according to the flux limiter function SUPERBEE [34].

3.1. Validation

For validation[1], a rectangular membrane area of 0.16×0.1 m^2 in the x and z direction is investigated according to the experiments performed by Banat [32]. In y-direction, the height of the hot feed and coolant channel is 1.5×10^{-3} m, of the air-gap 3.5×10^{-3} m and of the liquid film 0.5×10^{-3} m. In the hot feed and coolant channel, the computational domain consists of 92k cells, 215k in the air-gap domain and 31k in the liquid film. A grid sensitivity study has been performed concluding that a refined grid does not significantly change the results. Information about the mesh dimensions can be found in the appendix in Table A2. Gravity acts in the negative x-direction. The mean hot water and coolant inlet velocity is 0.6 m/s and a velocity profile is assumed which is parabolic in height and constant throughout the depth of the module. The coolant inlet temperature is 20°C. For the membrane, literature values for polyvinylidene fluoride (PVDF) are used for the thermodynamic properties. The membrane thickness is 110 μm, the pore diameter is 0.45 μm and the porosity is 75% [32]. The tortuosity is set to 1.5.

3.2. Orientation study

To study the influence on orientation, the layouts illustrated in Fig. 3 are modeled. The upside configuration equals the standard AGMD layout with the hot feed water flowing above the membrane (Fig. 3a). The results from the

[1]The source code can be found at https://github.com/kjcramer/pyns/tree/validation_study

validation study (Section 4.1) revealed that the temperature profile in the coolant channel has a minor impact on the MD process. Therefore, the coolant channel and the condensation surface separating the liquid film are excluded and instead, a constant temperature is assumed on the boundary of the liquid film and condensation surface.

In the downside configuration, the hot water channel and the air-gap are located below the membrane and the liquid film above the membrane (Fig. 3b). In this setup, the inverted temperature gradient is opposing gravity creating buoyancy which is expected to influence the heat and mass transfer in the module. Another feature of this setup is the air-gap separating feed stream and membrane. This reduces the contact of the membrane with contaminants and salt in the feed water, possibly reducing scaling and fouling which is a principal challenge in long-term operation [35].

In the hot water channel, a parallel velocity inlet profile is assumed. The investigated inlet velocities are 0.025, 0.05 and 0.1 m/s leading to volume fluxes of 1.05, 2.1 and 4.2 l/min. Inlet temperatures of 60°C, 70°C and 80°C are investigated. The Reynolds numbers are below 2,500 in all cases. The channel dimensions are 0.07 m × 0.07 m × 0.01 m adapting to ongoing experiments. Merck Millipore FGLP14250 is assumed as the membrane for the computations. Therefore, literature values for the thermal conductivity of polytetrafluoroethylene are used [36]. The membrane thickness is 65 μm, the porosity 85%, the pore diameter 0.2 μm and the tortuosity is 1.5. Membrane support grids that are used to ensure a constant air-gap thickness are not specifically modeled and their influence on the heat and mass transfer is assumed to be negligible. This assumption has been previously made in the CFD modeling of permeate gap membrane distillation [37] and also AGMD [19]. The air-gap thicknesses investigated in this study are 0.5×10^{-3}, 2×10^{-3} and 8×10^{-3} m. The liquid film is in upside configuration 0.5×10^{-3} m thick, in downside 1×10^{-3} m. The steel plate temperature is 15°C. In the downside configuration, no momentum exchange or shear is considered between feed water and air-gap[2].

For the computation, a Cartesian grid is chosen with 150k cells in the feed channel, 10k cells in liquid film in upside configuration, 20k cells in liquid film in downside configuration, 19k cells for smallest air-gap, 38k in medium air-gap and 150k cells in the largest air-gap. In comparison to a coarser grid, the permeate output and recovery ratio (RR) changed around 1% while the change in gained output ratio (GOR) was 4%. Therefore, the finer mesh was chosen for the computation. Information about the applied mesh can be found in the appendix in Table A3. As the dependency on the operational parameter of permeate output, RR and GOR were identical for both tested meshes, no further refinement was investigated.

3.3. Performance indicators

The RR relates the permeate mass flow $\dot{m}_{\text{permeate}}$ which is condensing into the liquid film, to the feed mass flow $\dot{m}_{\text{in}}$. The RR is calculated as:

$$\text{RR} = \frac{\dot{m}_{\text{permeate}}}{\dot{m}_{\text{in}}} = \frac{\dot{m}_{\text{permeate}}}{\rho u_{\text{in}} A_{\text{in}}} \tag{15}$$

where u_{in} is the feed inlet velocity and A_{in} the feed inlet area.

The GOR is a measure for the energy economization of the module indicating the heat used for evaporation of vapor as a fraction of the total heat input into the module $\dot{Q}_{\text{in}}$.

$$\text{GOR} = \frac{\dot{m}_{\text{permeate}} \cdot h_d}{\dot{Q}_{\text{in}}} = \frac{\dot{m}_{\text{permeate}} \cdot h_d}{\rho u_{\text{in}} A_{\text{in}} c_P \left(T_{\text{in}} - T_{\text{out}}\right)} \tag{16}$$

where h_d is the latent heat of vaporization, c_P the heat capacity and $(T_{\text{in}} - T_{\text{out}})$ the temperature difference in the feed channel between inlet and outflow averaged over the outflow area.

4. Results

4.1. Validation results

In Fig. 4 the permeate flux measured in the experiments by Banat [32] is compared to the condensation mass flux $\dot{m}_{\text{cond}}$ computed by the model. The permeate flux is increasing with increasing hot water inlet temperatures in both data sets and a good agreement can be found.

The validation process in this study follows the validation process by Alklaibi and Lior [13]. Interestingly,

Fig. 3. Illustration of the computed layouts and the coordinate systems; not to scale: (a) upside configuration and (b) downside configuration.

[2]https://github.com/kjcramer/pyns/tree/configuration_study

also their modeling results in a slightly higher mass flux at 50°C and 60°C while it shows a slightly lower mass flux at 40°C and 70°C comparing with the experimental values by Banat [32]. Validation data in tabular form can be found in Table A1.

In Fig. 5, the temperature profile is shown perpendicular to the membrane at different locations in the hot feed stream for the 70°C hot inlet temperature case. Variations are visible along the feed stream direction (x-direction). While close to the hot feed water inlet, a uniform temperature distribution can be seen in the hot salt water, a larger gradient becomes visible further downstream. This behavior can also be seen in the coolant channel in opposite direction and has been previously reported in the literature [13]. In the liquid film, however, the variation in temperature is reduced.

The temperature profile in the air-gap follows a concave slope at x = 0 m, a straight line in the middle and a convex slope on the hot water outlet side. These deviations from the straight profile are caused by natural convection occurring in the air-gap due to density differences and gravity. Natural convection in the air-gap has been reported previously by Chouikh et al. [14].

This temperature distribution leads to a profile of evaporation $\dot{m}_{mem}$ and condensation fluxes $\dot{m}_{cond}$ in x-direction as shown in Fig. 6. The membrane mass flux is increased at the hot feed water inlet due to the higher temperature gradient

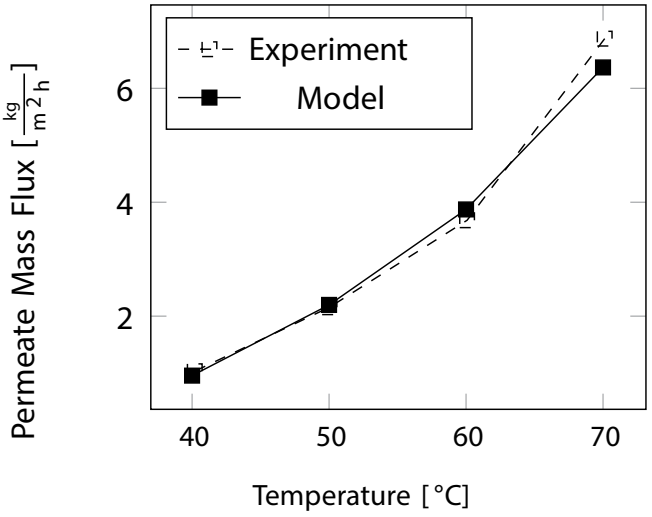

Fig. 4. Fresh water output for different hot salt water channel inlet temperatures; from the model the condensation mass flux $\dot{m}_{cond}$ is used, the experiments are performed by Banat [32].

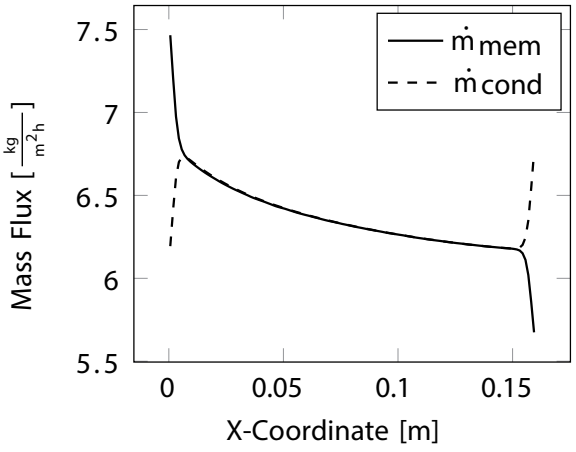

Fig. 6. Axial evaporation ($\dot{m}_{mem}$) and condensation mass flux ($\dot{m}_{cond}$) in mid z plane for 70°C hot inlet temperature.

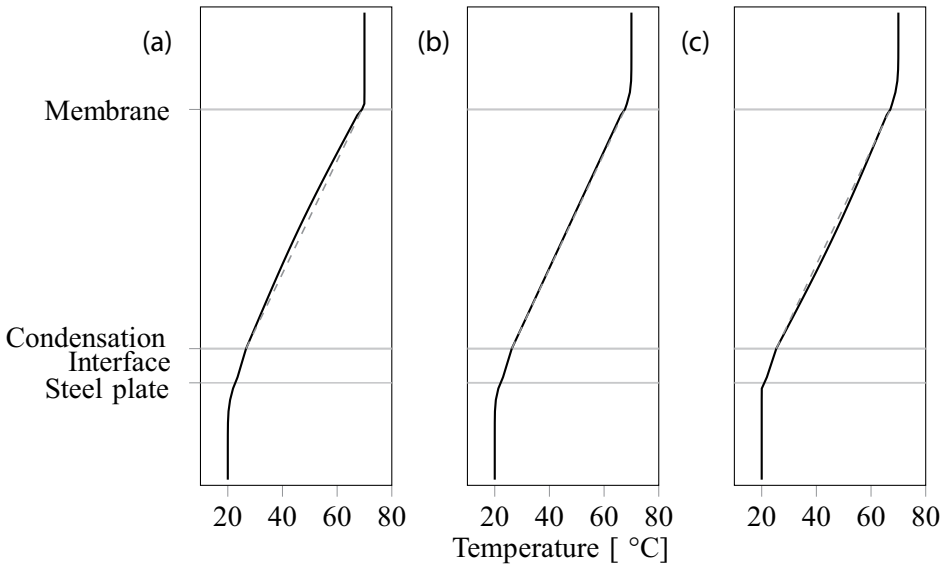

Fig. 5. The temperature profile in y-direction perpendicular to the membrane for 70°C hot inlet temperature (a) close to the hot water inlet (x = 0 m), (b) in the mid-X location (x = 0.8 m) and (c) close to the hot water channel outlet and the coolant inlet (x = 0.16 m); the dashed lines display a straight line between the temperatures at the membrane and at the condensation interface; deviations of the actual temperature profile (solid line) are due to natural convection.

across the membrane. Additionally, evaporation is favored by the natural convection loop counteracting sensible heat losses on this side. The opposite is occurring on the side of the hot water outflow, where the swirl reduces the heat available for evaporation, hence the sharp drop in evaporation mass flux.

The profile of the condensation mass flux in Fig. 6 is mainly influenced by the profile of the condensation interface $T_{\text{int,cond}}$ which is itself calculated by the vapor concentration a_{air} in the air-gap near the liquid film. $T_{\text{int,cond}}$ and a_{air}, therefore, have the same profile for small variations of $T_{\text{int,cond}}$ (Fig. 7). At the extreme x locations, the influence of the natural convection vortex on the vapor concentration leads to the sharp turns.

The temperature gradient across the membrane is reduced in comparison to the feed water and air-gap bulk temperature difference [Eq. (17)] [2,9].

$$\psi = \frac{T_{\text{int,evap}} - T_{\text{mem,bottom}}}{T_{\text{hot}} - T_{\text{air}}} \tag{17}$$

Temperature polarization values range from 0 to 1 where $\psi = 1$ means that no thermal boundary layer is established. By comparing different axial locations in Fig. 8, it can be seen that temperature polarization enhances flow direction and therefore depends on the channel geometry as reported previously [13].

A decline in the x-direction can be seen in many profiles: firstly in the evaporation interface temperature $T_{\text{int,evap}}$ and following also the temperature polarization ψ, the membrane flux $\dot{m}_{\text{mem}}$, the vapor concentration in the air-gap a_{air}, the condensation interface temperature $T_{\text{int,cond}}$ and finally the condensation mass flux $\dot{m}_{\text{cond}}$ (Figs. 6–8). Therefore, the evaporation interface temperature $T_{\text{int,evap}}$ displays the most influential variable and its optimization are crucial for the performance of the MD process.

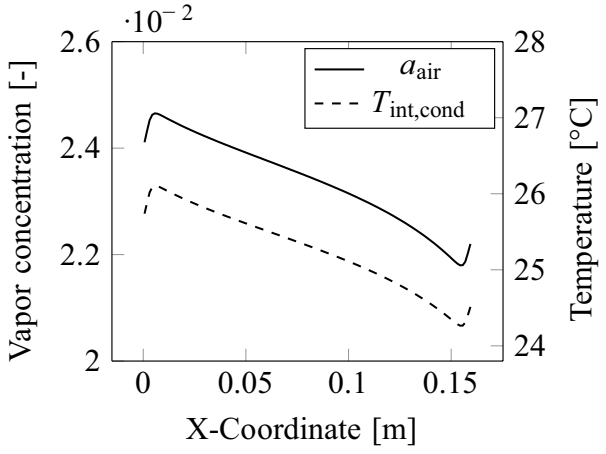

Fig. 7. Vapor concentration of air in the air-gap near the liquid film a_{air} and condensation interface temperature $T_{\text{int,cond}}$ in mid z plane for 70°C hot inlet temperature; as $T_{\text{int,cond}}$ is calculated from a_{air}, the curves are similar for small variations of $T_{\text{int,cond}}$.

4.2. Orientation study results

Fig. 9 shows the permeate flux plotted against the inlet velocity for different air-gap thicknesses and both configurations – upside and downside. The data proofs the strong dependence of the inlet temperature on the permeate flux as well as the weak dependence of the inlet flow velocity. This behaviour has been previously experimentally observed [38,39]. However, it can also be seen that the air-gap thickness has a similarly strong effect as the inlet temperature: a module operated at 80°C and 2 mm air-gap will produce the same permeate flux as a module operated at only 60°C and 0.5 mm air-gap.

Only small differences in permeate mass flux are found between upside and downside configuration. For the smallest air-gap (0.5 mm), the upside configuration produces a slightly higher permeate flux, while for the medium air-gap (2 mm) the permeate flux of the downside configuration is slightly increased. For the larger air-gap of 8 mm, no significant differences can be found. High inlet temperatures and feed velocities favor the upside configuration whereas the downside configuration is less susceptible to feed velocity changes and performs better at the lowest inlet velocity.

The same trends can be seen for the recovery ratio in Fig. 10, as the feed flow rate is independent of configuration, air-gap thickness and feed inlet temperature. Only, the effect of the feed inlet velocity is inverted and the RR is decreasing with increasing feed flow rate.

In Fig. 11 the GOR values are presented. For both configurations, GOR is increasing with increasing feed temperature and decreasing feed velocity which agrees with the literature [40]. A higher temperature leads to higher partial vapor pressure and therefore a higher driving force for the MD process. On the other hand, a higher feed flow rate increases the sensible heat transfer through the membrane which outweighs the gain in permeate flux at higher feed velocities and leads to a decreased GOR.

For the upside configuration, the influence of the air-gap thickness is less distinct and not consistent. A thicker air-gap reduces the sensible heat losses but also impairs the diffusive vapor transport which results in a smaller permeate flux as already shown in Fig. 9. The predominance is

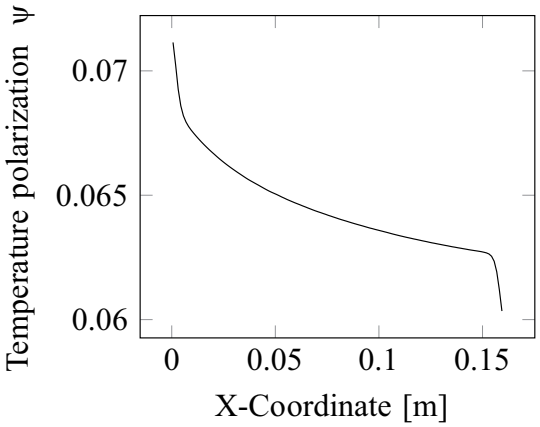

Fig. 8. Temperature polarization coefficient in mid z plane for 70°C hot inlet temperature.

changing in between the two effects for the largest air-gap (hence the crossing lines) but favors a thinner air-gap for the smaller air-gaps.

In the downside configuration, GOR is larger for smaller air-gaps indicating that the mass resistance increases stronger than the insulating benefits when enlarging the air-gap.

The GOR is consistently higher for the downside configuration indicating that less energy is needed to distill the same permeate flux compared to the upside configuration.

4.3. Flow field in the air-gap

Figs. 12 and 13 show the velocity fields in the air-gap of the downside configuration for different operational parameters. As the temperature gradient is opposing gravity, buoyancy effects can be seen. For T_{in} = 80°C and 8 mm air-gap (Fig. 12) vortexes are forming that are rotating alternately clockwise and counter-clockwise, generating thereby an upward or downward movement in between the swirls. The vortexes are uniform in z-direction and form

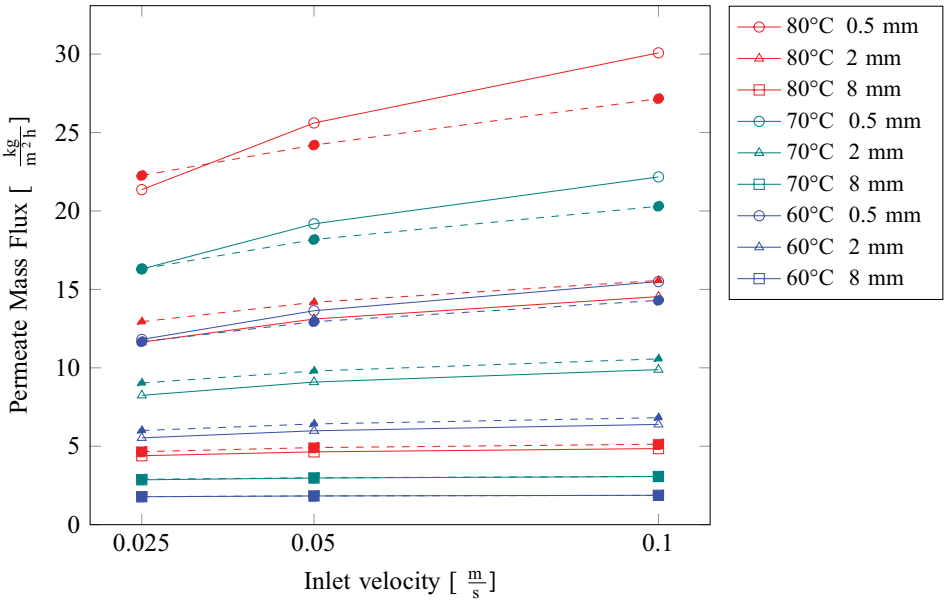

Fig. 9. Fresh water output for different hot channel inlet temperatures, velocities and air-gap thicknesses: —○— upside configuration; - ● - downside configuration.

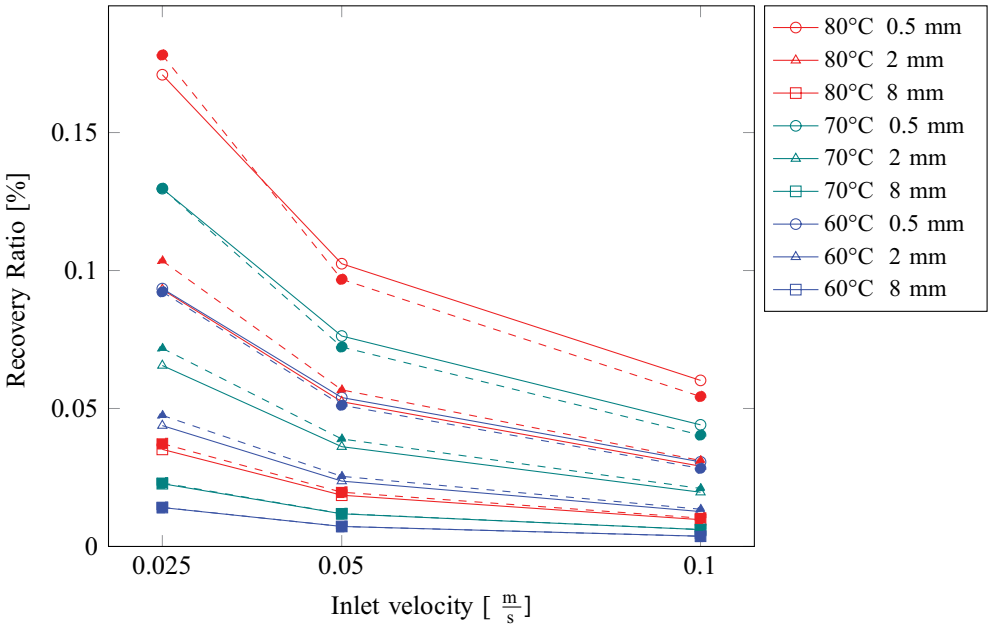

Fig. 10. Recovery ratio for different hot channel inlet temperatures, velocities and air-gap thicknesses: —○— upside configuration; - ● - downside configuration.

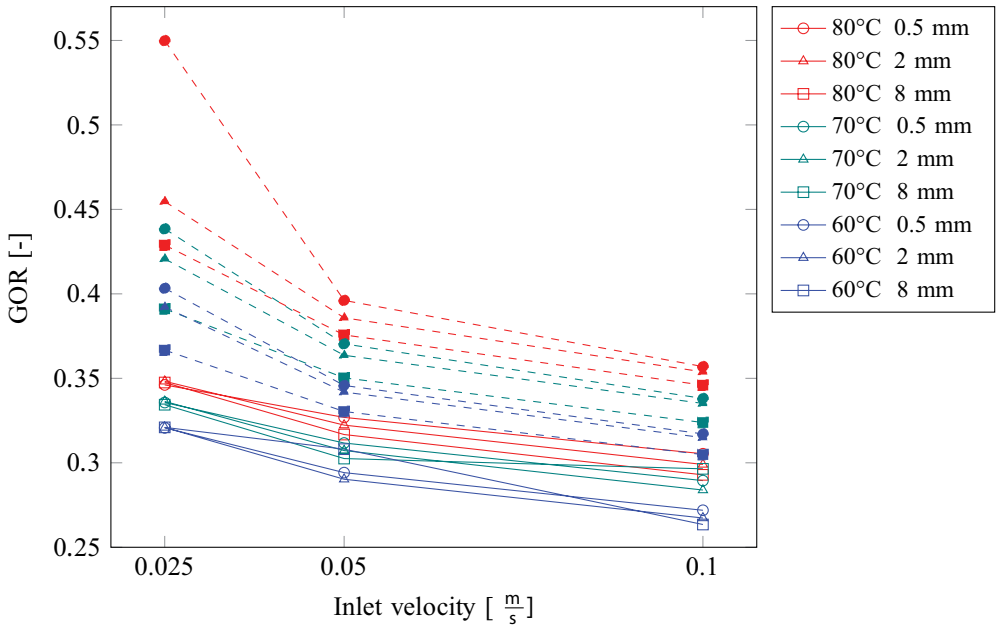

Fig. 11. GOR for different hot channel inlet temperatures, velocities and air-gap thicknesses: —○— upside configuration; - ● - downside configuration.

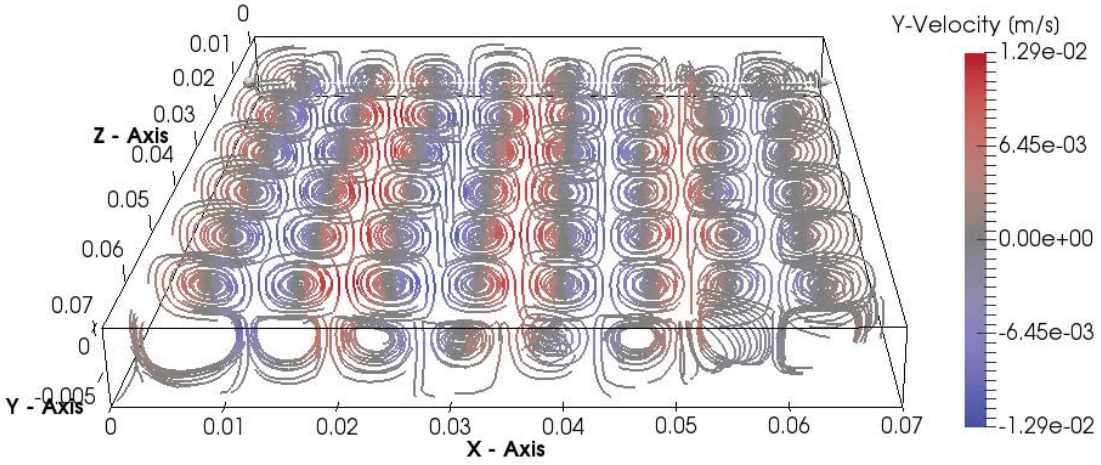

Fig. 12. Streamlines in air-gap for downside configuration, T_{in} = 80°C, u_{in} = 0.05 m/s and 8 mm air-gap.

along the *x*-axis, the direction of feed flow, for all analyzed inlet velocities.

For smaller air-gaps, no stationary vortexes are forming but nonetheless, a velocity field is observed with a vertical velocity component. Recalling the evaluation of the GOR in Fig. 11, the smaller air-gaps of the downside configuration performed best at minimizing sensible heat losses while still allowing for vapor mass transfer.

Fig. 13 shows the velocity fields for the slowest feed flow velocity (u_{in} = 0.025 m/s) at T_{in} = 70°C and 8 mm air-gap. Thereby, three fully established vortexes are visible. For faster inlet velocities, two are less established when increasing the feed velocity to 0.05 m and barely visible anymore for u_{in} = 0.1 m (Fig. 14). The favored formation of vortexes at lower feed velocities explains why the downside configuration is less susceptible to feed velocity changes. The vortexes encourage the mass transfer in the air-gap also at lower feed velocities.

For T_{in} = 60°C, no stationary swirls are observed, however, a distinctive vertical velocity component is still found.

5. Conclusion

A numerical model is introduced which computes AGMD modules in three dimensions covering the feed water channel, air-gap, liquid film and coolant channel. For evaporation and condensation, phase change energy conservation equations are solved. Thereby, the condensation mass flux is computed independently from the membrane mass flux. Simulation results are compared to experimental data and a good agreement is found.

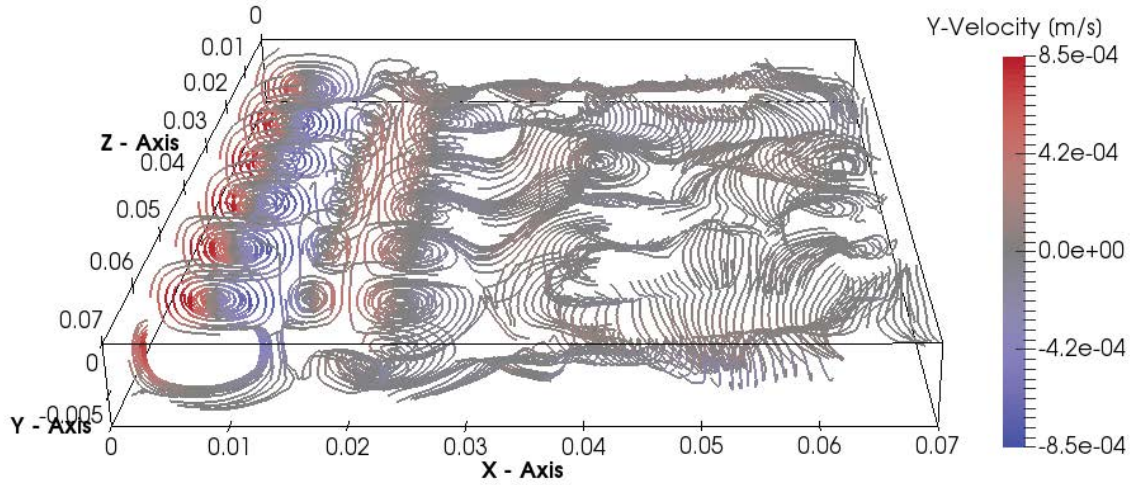

Fig. 13. Streamlines in air-gap for downside configuration, T_{in} = 70°C, u_{in} = 0.025 m/s and 8 mm air-gap.

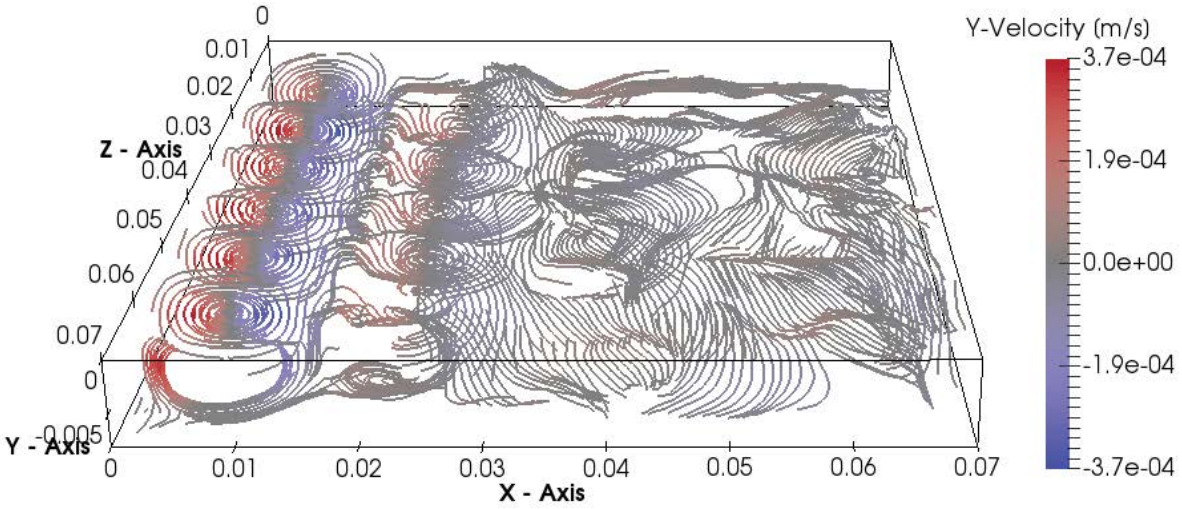

Fig. 14. Streamlines in air-gap for downside configuration, T_{in} = 70°C, u_{in} = 0.1 m/s and 8 mm air-gap.

The simulation results show flow profile variations in the axial direction and therefore the advantage of multi-dimensional calculations. Additionally, the uncoupling of the distillate mass flux from the membrane flux enables to study of gravitational effects and natural convection in the air-gap.

Two AGMD module configurations are numerically compared and their performance at different feed inlet temperatures, velocities and air-gap thicknesses evaluated. In the upside configuration, the hot feed flows above the membrane, while in the downside configuration it flows below the air-gap and membrane. In the latter, the feed solution is not in contact with the membrane but separated by the air-gap which is expected to improve the fouling resistance of the membrane. For the downside configuration, the velocity profile in the air-gap due to buoyancy is visualized.

The upside configuration produces a slightly higher permeate flux when combining a high feed inlet temperature (80°C), feed inlet velocity (0.1 m/s) and narrow air-gap (0.5 mm). At all other operational conditions, the permeate flux is comparable.

The downside configuration is less susceptible to feed inlet velocity than the upside configuration which shows in a slightly higher RR and evidently higher GOR at the lowest feed velocity studied. The vortex formation in the air-gap is favored by low feed velocities which result for smaller air-gaps in an increased energy utilization.

In general, the GOR is consistently and significantly higher for the downside configuration indicating that less energy is needed to distill the same permeate flux compared to the upside configuration. As the main advantage of AGMD is the reduction of heat losses, the downside configuration could bring further improvement in this direction.

Experiments are ongoing at the University of Luxembourg and the experimental validation of these findings is expected to be published soon.

Evaporation and scaling phenomena can be studied with ultra-high resolution fluid dynamic simulations [41,42]. For this purpose, three-dimensional structures have been obtained from membranes for MD by X-ray ptychography [43]. Insights from these studies shall benefit the development of the model towards prototyping MD modules for the treatment of highly saline brines for long-term operation.

Acknowledgments

We thank Dr. Thierry Baasch (Lund University) for comments on the manuscript and proofreading. The authors acknowledge ULHPC, Luxembourg for the computational resources. This study has been conducted in the scope of a dissertation at the University of Luxembourg [44].

References

[1] WHO, The Global Burden of Disease, Technical Report, WHO Press, World Health Organization, 20 Avenue Appia, 1211 Geneva 27, Switzerland (Tel. +41 22 791 3264; Fax: +41 22 791 4857; email: bookorders@who.int), 2008.
[2] A. Alkhudhiri, N. Darwish, N. Hilal, Membrane distillation: A comprehensive review, Desalination, 287 (2012) 2–18, (Special Issue in Honour of Professor Takeshi Matsuura on His 75th Birthday).
[3] A.M. Alklaibi, N. Lior, Membrane-distillation desalination: status and potential, Desalination, 171 (2005) 111–131.
[4] R.B. Saffarini, E.K. Summers, H.A. Arafat, J.H. Lienhard V, Economic evaluation of stand-alone solar powered membrane distillation systems, Desalination, 299 (2012) 55–62.
[5] M. Khayet, A. Velázquez, J.I. Mengual, Modelling mass transport through a porous partition: effect of pore size distribution, J. Non-Equilib. Thermodyn., 29 (2004) 279–299.
[6] K.W. Lawson, D.R. Lloyd, Membrane distillation, J. Membr. Sci., 124 (1997) 1–25.
[7] A.G. Fane, R.W. Schofield, C.J.D. Fell, The efficient use of energy in membrane distillation, Desalination, 64 (1987) 231–243.
[8] M. Khayet, Membranes and theoretical modeling of membrane distillation: a review, Adv. Colloid Interface Sci., 164 (2011) 56–88.
[9] R.W. Schofield, A.G. Fane, C.J.D. Fell, Heat and mass transfer in membrane distillation, J. Membr. Sci., 33 (1987) 299–313.
[10] S. Kimura, S.-I. Nakao, S.-I. Shimatani, Transport phenomena in membrane distillation, J. Membr. Sci., 33 (1987) 285–298.
[11] G.L. Liu, C. Zhu, C.S. Cheung, C.W. Leung, Theoretical and experimental studies on air-gap membrane distillation, Heat Mass Transfer, 34 (1998) 329–335.
[12] E.K. Summers, H.A. Arafat, J.H. Lienhard V, Energy efficiency comparison of single-stage membrane distillation (MD) desalination cycles in different configurations, Desalination, 290 (2012) 54–66.
[13] A.M. Alklaibi, N. Lior, Transport analysis of air-gap membrane distillation, J. Membr. Sci., 255 (2005) 239–253.
[14] R. Chouikh, S. Al Tahar Bouguecha, M. Dhahbi, Modelling of a modified air-gap distillation membrane for the desalination of seawater, Desalination, 181 (2005) 257–265.
[15] Z. Xu, Y. Pan, Y. Yu, CFD simulation on membrane distillation of NaCl solution, Front. Chem. Eng. China, 3 (2009) 293–297.
[16] J. Orfi, N. Loussif, P.A. Davies, Heat and mass transfer in membrane distillation used for desalination with slip flow, Desalination, 381 (2016) 135–142.
[17] I. Janajreh, D. Suwwan, R. Hashaikeh, Assessment of direct contact membrane distillation under different configurations, velocities and membrane properties, Appl. Energy, 185 (2017) 2058–2073.
[18] R. Schofield, A. Fane, C. Fell, Gas and vapour transport through microporous membranes. I. Knudsen- Poiseuille transition, J. Membr. Sci., 53 (1990) 159–171.
[19] I. Janajreh, K. El Kadi, R. Hashaikeh, R. Ahmed, Numerical investigation of air-gap membrane distillation (AGMD): Seeking optimal performance, Desalination, 424 (2017) 122–130.
[20] M.M.A. Shirazi, A. Kargari, A.F. Ismail, T. Matsuura, Computational Fluid Dynamic (CFD) opportunities applied to the membrane distillation process: state-of-the-art and perspectives, Desalination, 377 (2016) 73–90.
[21] I. Hitsov, T. Maere, K. De Sitter, C. Dotremont, I. Nopens, Modelling approaches in membrane distillation: a critical review, Sep. Purif. Technol., 142 (2015) 48–64.
[22] A. Bashirzadeh, B. Wu, Review of computational fluid dynamics simulation techniques for direct contact membrane distillation systems containing filament spacers, Desal. Water Treat., 162 (2019) 79–96.
[23] N. Tang, H. Zhang, W. Wang, Computational fluid dynamics numerical simulation of vacuum membrane distillation for aqueous NaCl solution, Desalination, 274 (2011) 120–129.
[24] X. Yang, H. Yu, R. Wang, A. Fane, Analysis of the effect of turbulence promoters in hollow fiber membrane distillation modules by computational fluid dynamic (CFD) simulations, J. Membr. Sci., 415–416 (2012) 758–769.
[25] K.C. Chong, S.O. Lai, K.M. Lee, W.J. Lau, B.S. Osi, A Study of Computational Fluid Dynamics on Membrane Module in Membrane Distillation, 2012 International Conference on Innovation Management and Technology Research, IEEE, Malacca, Malaysia, 2012, pp. 174–178.
[26] H. Hayer, O. Bakhtiari, T. Mohammadi, Analysis of heat and mass transfer in vacuum membrane distillation for water desalination using computational fluid dynamics (CFD), Desal. Water Treat., 55 (2015) 39–52.
[27] M. Hasanizadeh, P. Jafari, B. Farshighazani, M.K. Moraveji, CFD simulation of heat and mass transport for water transfer through hydrophilic membrane in direct-contact membrane distillation process, Desal. Water Treat., 57 (2016) 18109–18119.
[28] H. Chang, J.-A. Hsu, C.-L. Chang, and C.-D. Ho, CFD simulation of direct contact membrane distillation modules with rough surface channels, Energy Procedia, 75 (2015) 3083–3090.
[29] P. Yazgan-Birgi, M.I. Hassan Ali, J. Swaminathan, J.H. Lienhard V, H.A. Arafat, Computational fluid dynamics modeling for performance assessment of permeate gap membrane distillation, J. Membr. Sci., 568 (2018) 55–66.
[30] D.M. Warsinger, J. Swaminathan, L.L. Morales, J.H. Lienhard V, Comprehensive condensation flow regimes in air-gap membrane distillation: visualization and energy efficiency, J. Membr. Sci., 555 (2018) 517–528.
[31] Y.Z. Tan, L. Han, W.H. Chow, A.G. Fane, J.W. Chew, Influence of module orientation and geometry in the membrane distillation of oily seawater, Desalination, 423 (2017) 111–123.
[32] F.A. Banat, Membrane Distillation for Desalination and Removal of Volatile Organic Compounds From Water, Ph.D. Dissertation, McGill University, Montreal, Canada, 1994.
[33] O.C. Bridgeman, E.W. Aldrich, Vapor pressure tables for water, J. Heat Transfer, 86 (1964) 279–286.
[34] P.L. Roe, Characteristic-based schemes for the Euler equations, Annu. Rev. Fluid Mech., 18 (1986) 337–365.
[35] D.M. Warsinger, J. Swaminathan, E. Guillen-Burrieza, H.A. Arafat, J.H. Lienhard V, Scaling and fouling in membrane distillation for desalination applications: a review, Desalination, 356 (2015) 294–313.
[36] Engineering ToolBox, Thermal Conductivity of Common Materials and Gases, 2003. Available at: https://www.engineeringtoolbox.com/thermal-conductivity-d_429.html
[37] P. Yazgan-Birgi, M.I. Hassan Ali, J. Swaminathan, J.H. Lienhard V, H.A. Arafat, Computational fluid dynamics modeling for performance assessment of permeate gap membrane distillation, J. Membr. Sci., 568 (2018) 55–66.
[38] F.A. Banat, J. Simandl, Desalination by membrane distillation: a parametric study, Sep. Sci. Technol., 33 (1998) 201–226.

[39] G.L. Liu, C. Zhu, C.S. Cheung, C.W. Leung, Theoretical and experimental studies on air-gap membrane distillation, Heat Mass Transfer, 34 (1998) 329–335.
[40] R.B. Saffarini, E.K. Summers, H.A. Arafat, J.H. Lienhard V, Technical evaluation of stand-alone solar powered membrane distillation systems, Desalination, 286 (2012) 332–341.
[41] N.I. Prasianakis, E. Curti, G. Kosakowski, J. Poonoosamy, S.V. Churakov, Deciphering pore-level precipitation mechanisms, Sci. Rep., 7 (2017) 13765, doi: 10.1038/s41598-017-14142-0.
[42] S.V. Churakov, N.I. Prasianakis, Review of the current status and challenges for a holistic process-based description of mass transport and mineral reactivity in porous media, Am. J. Sci., 318 (2018) 921–948.
[43] K. Cramer, N.I. Prasianakis, B. Niceno, J. Ihli, M. Holler, S. Leyer, Three-dimensional membrane imaging with X-ray ptychography: determination of membrane transport properties for membrane distillation, Transp. Porous Media, 138 (2021) 265–284.
[44] K. Cramer, Numerical modeling of air-gap membrane distillation, Ph.D. Dissertation, University of Luxembourg, Luxembourg, Luxembourg, 2019.

Appendix

Table A1
Validation data; standard deviation is 0.27

Hot inlet temperature (°C)	40	50	60	70
Mass flux Banat [32] (kg/m²h)	1.033	2.156	3.682	6.871
Mass flux simulation (kg/m²h)	0.956	2.197	3.873	6.366
Absolute difference (kg/m²h)	–0.077	0.041	0.190	–0.505
Relative difference (%)	–7.4	1.9	5.1	–7.3

Table A2
Grid information for validation study

	# cells	Cell dimensions in subdomain		
		X (m)	*Y* (m)	*Z* (m)
Hot water channel	92k	6.667e-4	1.500e-4	6.667e-4
Air-gap	215k	6.667e-4	2.917e-4	6.667e-4
Liquid film	31k	6.667e-4	1.667e-4	6.667e-4
Coolant channel	92k	6.667e-4	1.500e-4	6.667e-4

Table A3
Grid information for orientation study

	# cells	Cell dimensions in subdomain		
		X (m)	*Y* (m)	*Z* (m)
Hot water channel	150k	1.25e-3	2.083e-4	1.25e-3
Air-gap 8 mm	150k	1.25e-3	1.667e-4	1.25e-3
Air-gap 2 mm	38k	1.25e-3	1.667e-4	1.25e-3
Air-gap 0.5 mm	19k	1.25e-3	8.333e-5	1.25e-3
Liquid film	10k/20k	1.25e-3	1.667e-4	1.25e-3